











Selection and Characteristics of the Dragonfly Landing Site near Selk Crater, Titan

Ralph D. Lorenz¹ , Shannon M. MacKenzie¹ , Catherine D. Neish^{2,3} , Alice Le Gall⁴ , Elizabeth P. Turtle¹ ,
Jason W. Barnes⁵ , Melissa G. Trainer⁶ , Alyssa Werynski², Joshua Hedgepeth², and Erich Karkoschka⁷ 

¹ Johns Hopkins University Applied Physics Laboratory 1001 Johns Hopkins Road, Laurel, MD 20723, USA

² Department of Earth Sciences, The University of Western Ontario, London, Canada

³ The Planetary Science Institute, Tucson, AZ, USA

⁴ LATMOS/IPSL, UVSQ Université Paris-Saclay, Sorbonne Université, CNRS, Paris, France

⁵ Department of Physics, University of Idaho, Moscow, ID 83844-0903, USA

⁶ NASA Goddard Space Flight Center, Greenbelt, MD, USA

⁷ Lunar and Planetary Laboratory, The University of Arizona, Tucson, AZ, USA

Received 2020 September 21; revised 2020 November 30; accepted 2020 December 2; published 2021 February 8

Abstract

The factors contributing to the initial selection of a dune site near the Selk impact structure on Titan as the first landing site for the Dragonfly mission are described. These include arrival geometry and aerodynamic/aerothermodynamic considerations, illumination, and Earth visibility, as well as the likely presence of exposed deposits of water-rich material, potentially including materials where molten ice has interacted with organics. Cassini observations of Selk are summarized and interpreted: near-infrared reflectance and microwave emission data indicate water-rich materials in and around the crater. Radar topography data shows the rim of Selk to have slopes on multi-km scales reaching only $\sim 2^\circ$ degrees, an order of magnitude shallower than early photoclinometric estimates.

Unified Astronomy Thesaurus concepts: [Saturnian satellites \(1427\)](#)

1. Introduction

Dragonfly is a relocatable lander destined for Titan (Lorenz et al. 2018; Turtle et al. 2018) selected in 2019 as the fourth mission in NASA's New Frontiers Program. Exploiting Titan's dense atmosphere and low gravity, Dragonfly uses a multi-rotor mobility system to explore diverse sites over tens to hundreds of kilometers.

The scientific motivation for Dragonfly is to determine the composition of surface materials where prebiotic chemistry is expected to be most advanced. Of particular interest are cryolava flows or in impact melt deposits. Laboratory studies have shown that Titan haze analogs quickly hydrolyze to yield known building blocks of life, such as amino acids and nucleobases (e.g., Neish et al. 2008, 2009, 2010). Neish et al. (2018) note that impact melts will likely have encountered higher temperatures (273 K and above) than cryolava deposits (perhaps little higher than 176 K). Chemical kinetics would lead to orders of magnitude higher reaction rates, and thus much richer prebiotic synthesis, in the impact melt case.

The present paper lays out the geometrical aspects of Dragonfly's arrival which defined the accessible area on Titan and why the Selk impact structure and nearby dune fields were selected as the most promising scientific targets. The Cassini data available on Selk and its environs are summarized, and how this information was used during Dragonfly's initial formulation and Phase A study (2016–2019) to define the initial landing site. It should be recognized that the Dragonfly mission is still undergoing detailed definition (Phase B) and some minor details, such as the exact dimensions and position of the landing ellipse, are subject to ongoing and future refinement. It should be understood also that this paper is not

intended to offer a comprehensive or final interpretation of Cassini data of the Selk region, but rather to motivate more detailed studies.

1.1. Requirements

The scientific goals above for Dragonfly indicate desired aspects of the destination region. As discussed in Lorenz (2019), the provision of mobility permits partial decoupling of the scientific desirability of a target site from the topographic features of a site for safe landing. An obvious implicit requirement for a successful mission is that safe landing terrain exists. Precedent from lunar and Mars exploration (e.g., Golombek et al. 2003) argues that characteristics defining safety are slopes less than 10° – 15° , and a low probability of encountering obstacles (“rocks”) on a lander scale (~ 1 m). Geological analogy suggests that dune fields are highly probable to satisfy these criteria. While steeper slopes can obviously exist on dune slip faces, these are readily detected and avoided, and interdune flats are ideal for landing as sand may partly mantle any gullies or rocks. It may be recalled that mantling was considered a reassuring consideration in Viking landing site definition, as being likely to diminish crater or other slopes, e.g., Masursky & Crabill (1976). Another implicit, but notable, constraint is that adequate data exist at a candidate landing site to assert it as being suitable—it should be remembered that Titan radar coverage at 1 km resolution or better only amounts to about 40% of the surface, and other Titan data sets are even more limited.

The limited available resolution of remote sensing data at Titan puts landing site identification at Titan today on a somewhat analogous footing as the identification of the Viking lander sites in 1976, e.g., Stooke (2012): large scale landforms can be identified and the relevant geological processes deduced, but the lander-scale terrain characteristics must be estimated by geological analogy and with some limited



Original content from this work may be used under the terms of the [Creative Commons Attribution 4.0 licence](#). Any further distribution of this work must maintain attribution to the author(s) and the title of the work, journal citation and DOI.

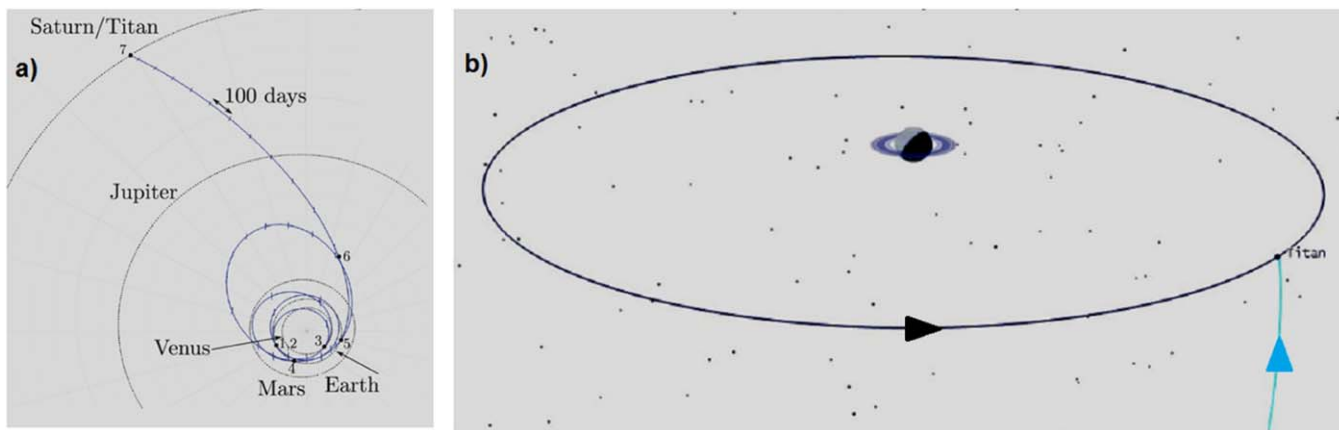


Figure 1. (a) Phase A interplanetary trajectory with launch in 2025 and Titan arrival in 2034. The launch date has since been prescribed to be 2027, although the arrival date and conditions remain the same. (b) Titan arrival in a Saturn-fixed frame (the arrival direction thus is now rotated relative to (a) as the vector difference of the interplanetary heliocentric arrival velocity and Saturn’s orbital velocity). The vehicle is aimed at the trailing hemisphere of Titan, to minimize the entry velocity. The resultant arrival direction defines the hemisphere accessible to Dragonfly.

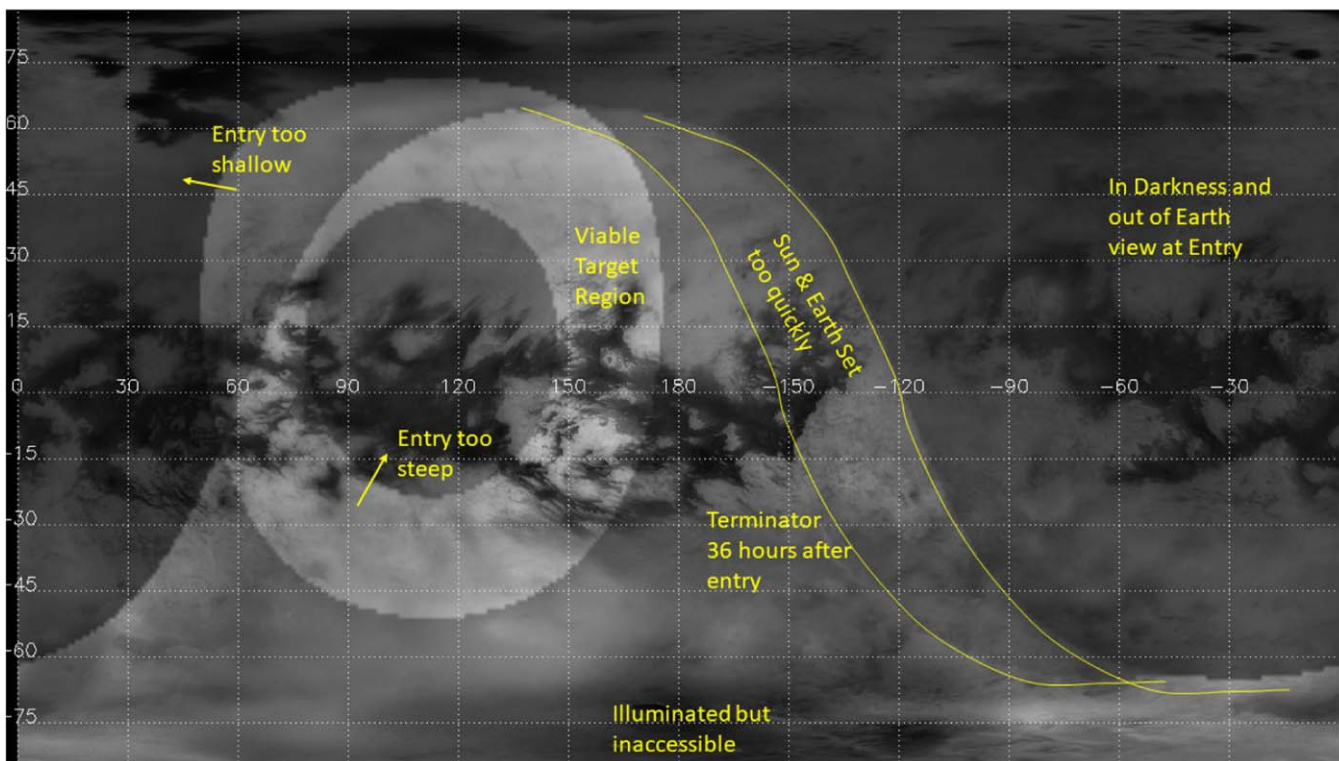


Figure 2. Schematic illustration of the combined delivery constraints. Given the incoming direction on a given epoch, the aerodynamic/aerothermodynamic constraints define a toroidal region where the flight path angle is in an allowable range. To perform descent while in Earth communication and with illumination requires being on the dayside at entry. Requiring a period of some days on the ground before sunset eliminates the late afternoon sliver of the daylight region. The logical AND combination of the entry and illumination constraints defines the accessible region for that entry epoch. The accessible regions for a range of arrival epochs (defined by the allowable Titan-relative entry velocity) can be combined in a logical OR sense to yield the ultimate set of possible target locations.

quantitative constraints from radar data and scattering models. Although some large rocks proved to exist at both sites, e.g., “Big Joe” near Viking 1, and Viking 2 had one landing foot somewhat perched, both Vikings landed successfully. The contemporary Mars site selection process (e.g., Golombek et al. 2003) exploits global high-resolution high-precision data sets on slope, topographic roughness, rock abundance etc. which are simply not available for Titan until a future orbiter mission performs comparable mapping.

There are geometric constraints associated with any specific mission opportunity, specifically landing date. Landing during polar winter places severe restriction on science operations that might require illumination (notably, mobility) (Barnes et al. 2020), and prevents direct-to-Earth communication and so would require a much more expensive architecture with a relay spacecraft. In the context of the New Frontiers 4 competition, which specified launch in 2025 (and thus, in practical terms, arrival in the mid-2030s during northern winter) this precluded

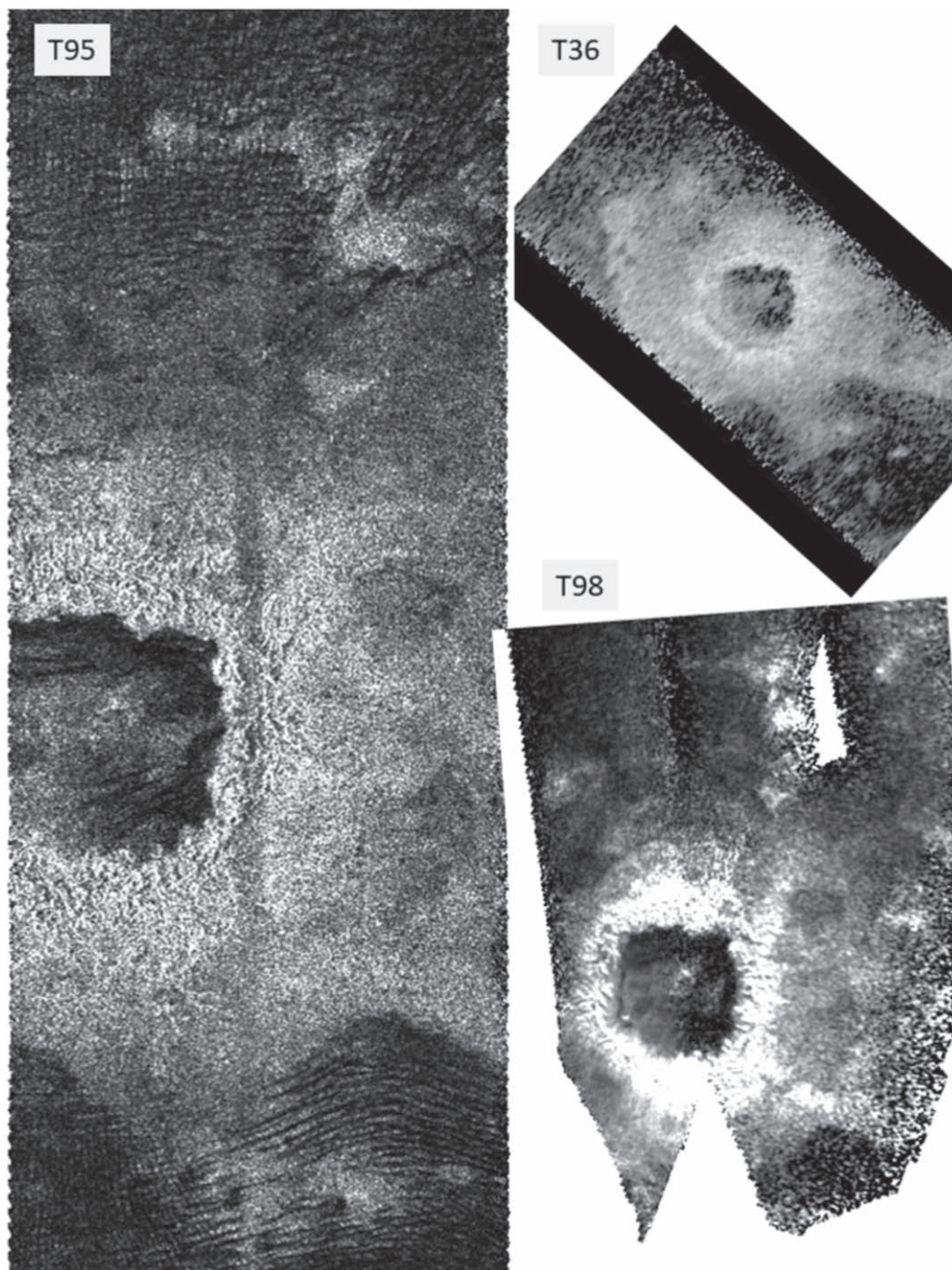


Figure 3. SAR imaging of Selk. The T95 SAR swath is the highest resolution data available (300×390 m). The incidence-corrected backscatter product ID on the PDS is [BIFQI09N199_D253_T095S01_V02](#). Heavy dissection of the rim is evident, and a few dunes appear to be present on the crater floor. To the south, linear dunes taper out and re-emerge. The general E-W alignment of linear dunes seen all over Titan is prominent at right, although a second orthogonal set is present at left: this may be a result of “flow-straightening” by the crater causing a transverse dune pattern. The dune pattern to the north is predominantly E-W linears but with some irregularities. The T36 image is of considerably lower quality. The T98 image (lower right) is of superficially low quality but highlights roughness around the rim.

exploration of Titan’s northern seas as in the proposed Titan Mare Explorer (TiME) mission (Stofan et al. 2013).

Additional geometric constraints emerge from implementation choices in a mission concept. First, a single-element in situ mission at Titan should logically take advantage of Titan’s atmosphere for entry directly from the interplanetary arrival trajectory, avoiding the need for propulsive orbit insertion. Atmospheric entry speed and angle, together with the ballistic coefficient (mass/area ratio) of the aeroshell, determine the peak deceleration (g-load), peak heating rate, and total heat

load that the vehicle must tolerate. Programmatic choice of aeroshell diameter, in turn limited by launch vehicle fairing size, and of thermal protection system (TPS) material on the heat shield, will in turn map to constraints on entry speed. Because the arrival velocity of the spacecraft in the Saturnian system adds vectorially with Titan’s orbital motion, it is therefore preferred to aim at Titan’s trailing hemisphere i.e., 180–360 west Longitude, since Titan’s orbital motion subtracts from the arrival speed (Figure 1). How far from centered on the trailing hemisphere the incoming asymptote can be depends on



Figure 4. T120 SAR imaging of Selk, overlain on the ISS mosaic. This image (generated with the convenient web tool TitanTrek (<https://trek.nasa.gov/titan/>)) shows the “fingers” of SAR data at the end of the swath. These may merit closer examination in further work.

the available TPS and other factors. In practice, the entry flight path angle from horizontal is unlikely to be at 90° (centered on the asymptote) but at some shallower angle to spread the energy dissipation over a longer path. The Huygens probe had an entry angle of 65° , and for heritage reasons it was chosen to limit the angle to a similar range. These entry dynamics and aerothermal constraints define a broadly toroidal region on Titan that can be accessed.

A final factor is the visibility of entry. NASA guidelines require that critical events such as entry, descent, and landing (EDL) be monitored in real time and thus (absent any relay assets at Saturn) be in direct line-of-sight to Earth. Although formally one could be compliant by landing at the terminator (Earth and Sun are within a few degrees of each other as seen from Titan) a prudent mission would require a 2–3 of days of Earth visibility after landing to ensure safe landing and early operations before entering Titan night and communications blackout of 8 days. Given Titan’s rotation period of 16 days (22.5 day^{-1}) the landing site should be $\sim 70^\circ$ west of the sunset terminator (Figure 2). The formulation of the original (2016) Dragonfly trajectory and arrival geometry subject to these geometric factors with a launch anticipated in 2025 is discussed in Scott et al. (2018). It should be noted that trajectory redesign is presently underway for a planned 2027 launch date, so many details of the mission are subject to modest revision. The broad geometric considerations, and target geological location, are unlikely to change, however.

In the absence of knowledge of the surface, delivery geometry considerations were the principal factors determining the original entry and descent location of the Huygens probe (Ott 1992). The probe had to be retargeted after the discovery of a design flaw in the radio link, and again illumination, aerothermodynamics, and relay link geometry were the main factors (e.g., Lebreton et al. 2005), although by this time some

information on surface albedo patterns was available from Hubble maps and other observations. It was known that the targeted region was the border between bright and dark regions, but its nature was unknown.

1.2. Site Selection

Informed by the gross constraints and intent described in the previous section, the core science team examined a suite of possible landing locations. It was quickly determined (Figure 2) that the Selk impact crater was the most obvious site of possible water-organic interaction within the feasible landing locus. A more careful examination confirmed that water-rich material was exposed in and around the crater, as indicated by Cassini Visual and Infrared Mapping Spectrometer (VIMS) data (e.g., Soderblom et al. 2010) and that good radar coverage existed. Selk has been observed in synthetic aperture radar (SAR) mode several times, including one swath with high resolution that yielded several topographic tracks (Stiles et al. 2009) across the crater and its ejecta blanket (these data are discussed in a later section. Importantly, extensive dunes can be identified around the crater, making an initial safe landing possible with subsequent transit to Selk.

2. Available Data on Selk and Interpretation

The Selk impact structure was visible as a bright spot in Cassini Imaging Science Subsystem (ISS) near-infrared observations ($0.938 \mu\text{m}$) acquired in the first Titan flyby TA in 2004 October (see upper left of Figure 4 of Porco et al. 2005). As for many other bright spots, Selk was targeted during long-range “HiSAR” radar observations for follow-up investigations. A HiSAR observation was executed on flyby T36 in 2007, revealing Selk as an 80 km crater (Wood et al. 2010; Neish & Lorenz 2012). This interpretation is corroborated by

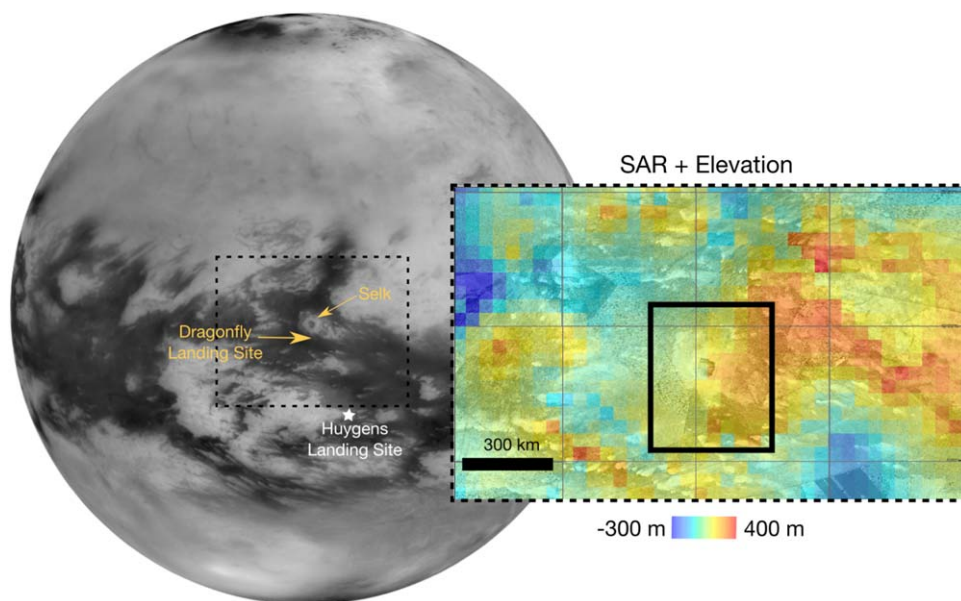


Figure 5. Orthographic projection of ISS data (Karkoschka et al. 2017) for Selk-centered hemisphere. (dashed inset) SAR regional mosaic colored with elevation data from Corlies et al. (2017). The solid black outline indicates the extent of area around Selk analyzed in Section 2 and shown in Figures 4, 7–11.

VIMS data on Selk acquired in T35, T37, T38, and T40 in 2007–2008 (Soderblom et al. 2010). (Succeeding VIMS observations (e.g., T70, T79, T85, T88) are not of as high spatial resolution as the prime mission data.) Furthermore, Selk was noted by Janssen et al. (2016) as a site with locally low microwave emissivity forming a low-brightness temperature ring around the crater, a characteristic associated with some other impact structures. The favored interpretation was that the impact has excavated ice-rich material from depth, thus resulting in locally enhanced volume scattering.

Soderblom et al. (2010) attempted a photoclinometric (“shape from shading”) interpretation of the VIMS data. Such methods rely on assumed uniform photometric properties of the surface material (unlikely in complex terrain) and are also challenged by atmospheric effects. They derived radial profiles of the rim/blanket topography, suggesting it rose and fell by 3–5 km over 30–40 km transects, indicating slopes of around 20° over 10 km length scales.

These results appear to be refuted by high-resolution SAR data acquired in the T95 flyby on DOY 287 of 2013 (Figure 3). The image segment at Selk has a representative azimuth resolution of 300 m and a range resolution of ~ 400 m (West & Veeramachaneni 2014), the exact values varying across the scene. The correlation between the subswaths acquired by the 5 radar beams allows recovery of a topographic profile (“SARtopo,” Stiles et al. 2009; Neish et al. 2018), with an effective resolution of 5–10 km. The T95 swath in the nominal incidence angle profile would have passed near the crater, but the pointing was adjusted specifically to image the crater better. The T95 SAR observation is considered the definitive morphological data set on Selk, having good geometric control and the best resolution. Note that the georeferencing of Cassini remote sensing data, and any targeting based thereon, may require adjustment in 2034 depending on the Titan rotation model adopted at that time (e.g., Hofgartner et al. 2020), but the correction is likely to be only of the order of a few km at most.

Selk was also imaged at the edge of a HiSAR observation on T98: although the resolution of this observation is poorer, it is at a rather more shallow incidence angle, giving independent

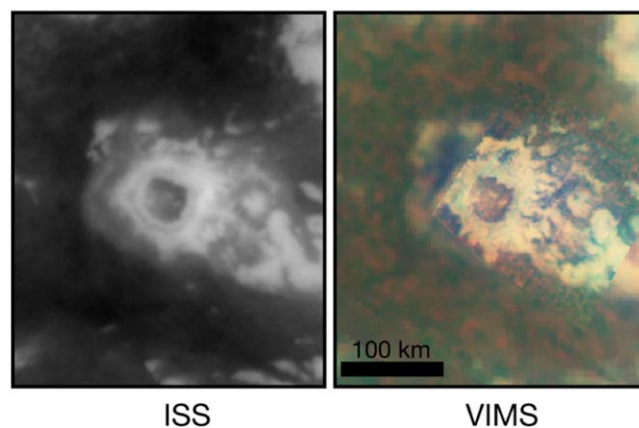


Figure 6. ISS and VIMS mosaics used to classify the terrain in Figures 9 and 10. The ISS mosaic was created from hundreds of individual images by Karkoschka et al. (2017). The VIMS image is a mosaic from T35, T37, T38, and T40 flybys and colored such that R, G, B = 5, 2, 1.3 μm .

information on surface properties. On flyby T120 (Figure 4), Selk was targeted during a ridealong observation (where the RADAR instrument did not control pointing): ambiguity errors due to the off-optimal incidence angle mean that the recoverable beam subswaths do not overlap, so only a couple of narrow strips of data cross the Selk region. Finally, a HiSAR imaging segment was acquired on flyby T121. This segment (T121S06) of the observation, not shown in the present paper, is only modest in quality (between the T98 and T36 images) but may have value in that it covers the region around Selk without large gaps. Unfortunately, no Cassini radar altimeter data exist directly over this area, although examination of altimeter echoes (e.g., Le Gall et al. 2011) over terrains elsewhere that have other characteristics (such as SAR morphology) to the Selk region may prove instructive.

For Dragonfly mission planning, a surface classification map was developed from each of the SAR, ISS, and VIMS data sets (Figures 5 and 6) in quarter-degree (~ 10 km) grid cells. This

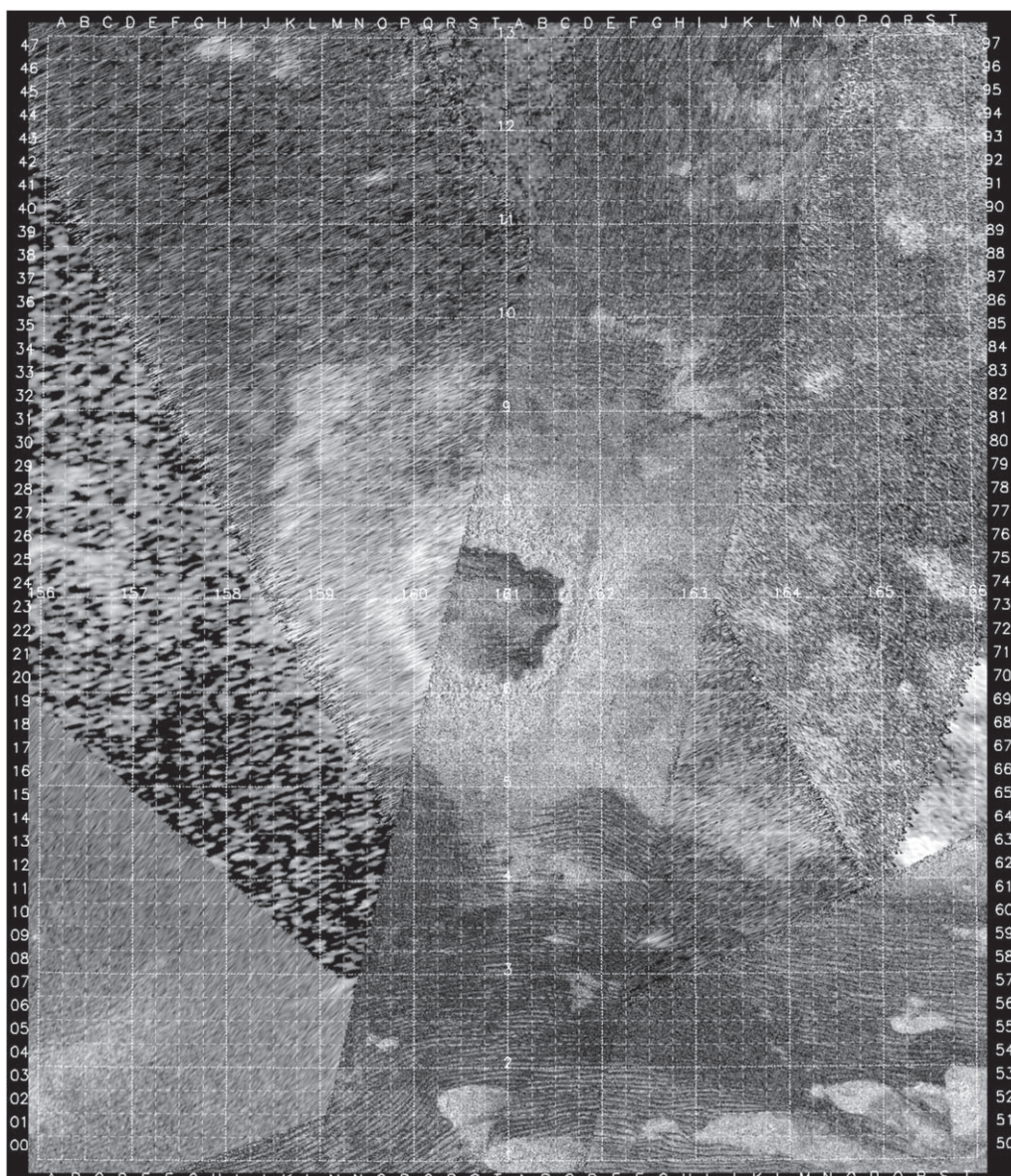


Figure 7. Radar mosaic of the Selk Region for terrain classification in Section 2.1. Latitude and Longitude scales are indicated on the central axes: grid cells can be referred to by a unique three-character code Lnn where L is the letter indicating east–west, and nn the north–south where nn < 50 refers to the west half of the grid and nn > 50 to the east. Note that individual dunes are well-resolved in the lower right part of the mosaic.

resolution was chosen as a reasonable compromise between giving adequate fineness for targeting, providing enough pixels per cell to permit geomorphological interpretation (e.g., the 400 m radar resolution indicated above should not be taken to imply the ability to recognize features of this size, speckle noise being an important additional consideration), and requiring a manageably small number of cells to evaluate over the target domain. The targeting has been performed based on morphology and analogs alone. Quantitative interpretation of reflectivity properties in terms of surface models must be done with caution (as the photogrammetry experience indicates) and is left for future work. To facilitate further analyses, we have made available a number of products from the present paper online at the JHU-APL Data Archive.⁸

2.1. SAR Morphology

Analysis of the SAR map of Figure 7 resulted in eight classification units, shown in Figure 8, which are consistent with the general morphological classification schema for Titan (e.g., Lopes et al. 2019). The SAR data are best for morphological distinctions given the spatial resolution of up to 300 m, but gaps in the data set prohibit classification of the full map (“0” in Figure 7). Areas with clear dune-interdune boundaries (“1”) are identifiable by a dark-bright pattern where dark lines are the organic sands and bright lines are interpreted as sand-free interdunes. A radar-dark surface may represent sandy interdunes (and thus minimal dune-interdune contrast) or be a function of insufficient resolution (“4”).

The crater floor is identifiable in SAR data as bright with no obvious ridge or slope textures—bright/dark pairings—like those of Titan’s mountains Radebaugh et al. (2007) located within the crater rim (“5”). Selk’s ejecta blanket shares similar

⁸ <http://lib.jhuapl.edu/>

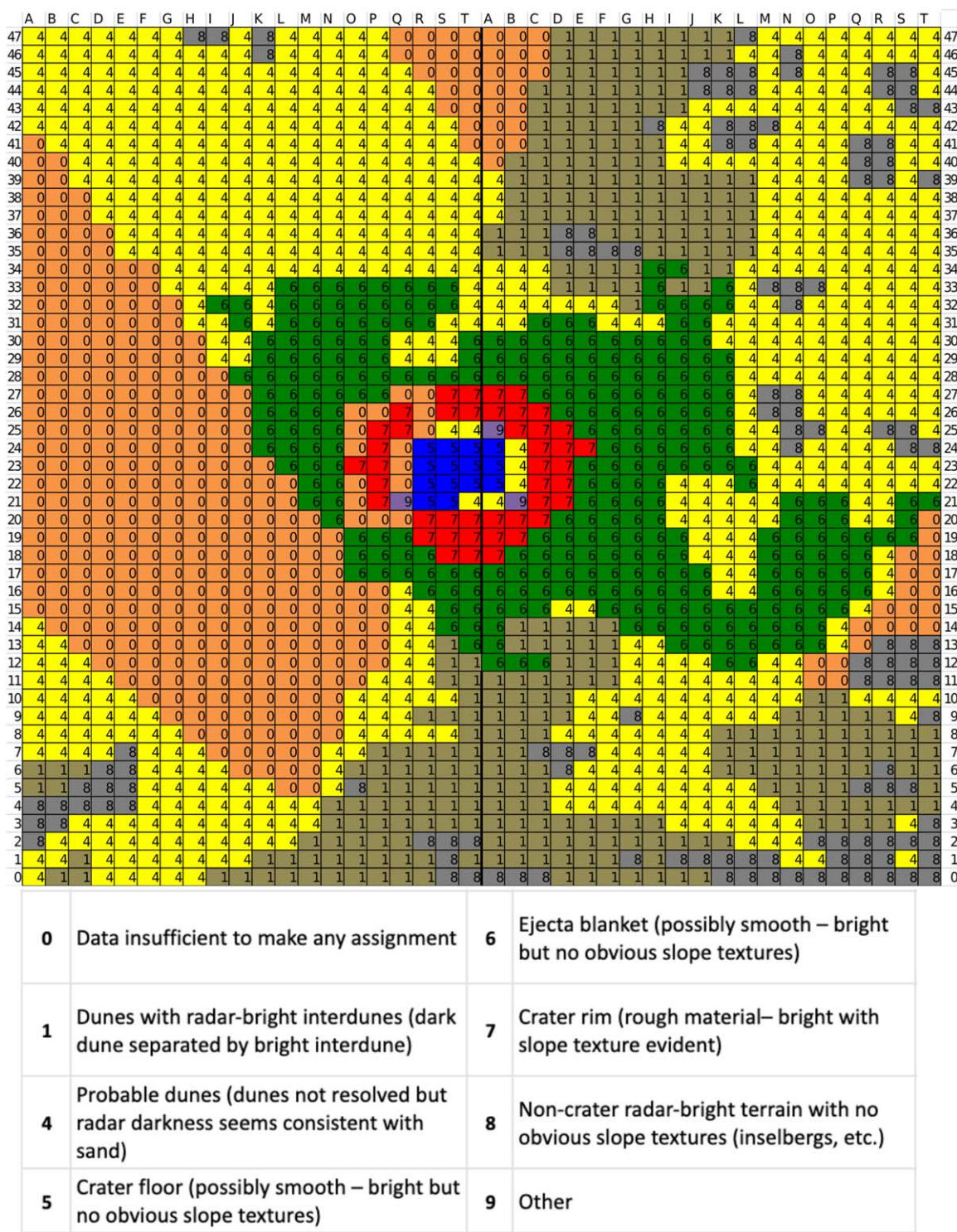


Figure 8. SAR classification map and units. (Nonsequential numbering is a result of unused units).

characteristics—bright without slope texture—but is located outside of the crater rim (“6”), extending southeastward. There are areas smooth at the 2 cm scale within the crater floor and ejecta, indicated by the lack of texture in SAR observations. These areas, some of which may be sand-covered, make promising targets for landing and sampling. Highly textured, bright SAR returns indicate rough material at the 2 cm scale. Forming a roughly circular pattern, these mark the crater rim (“7”). Other radar-bright terrain without slope textures and

located away from the crater (e.g., inselbergs) are also in the scene (“8”). Only a few grid cells fell outside of any of these categories (“9”).

2.2. VIMS Spectral Characteristics

Data from Titan flyby T40 represent the best VIMS observations of Selk and are publicly available from the PDS (cubes CM_1578264152_1, CM_1578263500_1, and CM_1578263152_1). These data have a resolution of

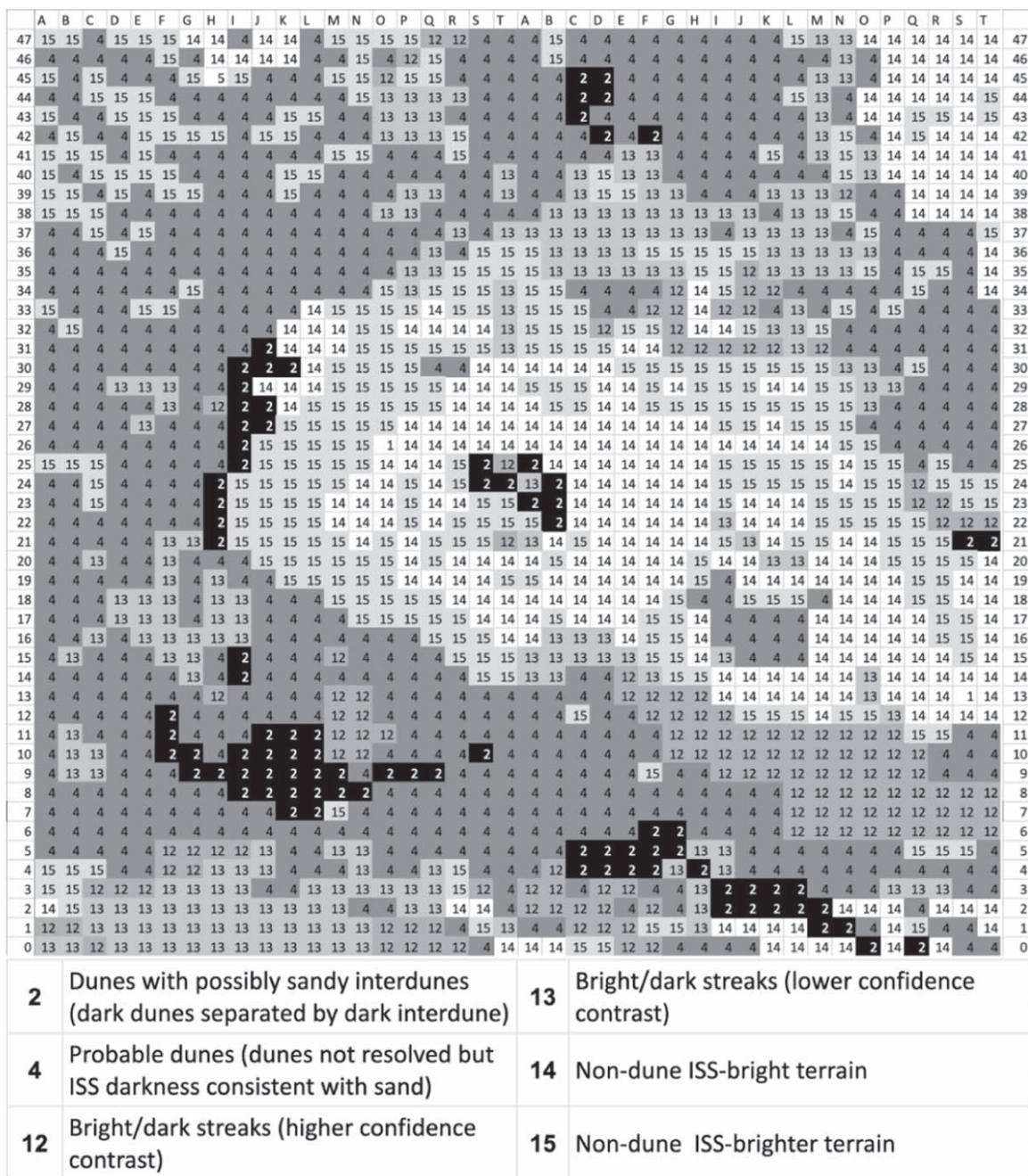


Figure 10. ISS classification. As in VIMS data, the organic sand have low reflectance. Linear, dark morphologies separated by bright areas likely represent dunes and sand-free interdunes (“12” and “13” where the later are at the limits of confidence), but not all cases are as clear. Some dunes are at the limit of distinguishability, perhaps indicating sandy interdunes (“2”) or just insufficient resolution (“4”). Bright terrains are classified at two levels (“14” and “15”), which may reflect differences in composition or surface roughness properties.

grid as RADAR and VIMS data for this work. The result was interpreted based on morphology and reflectance (Figure 10).

As in VIMS data, organic sand appears dark to ISS and the crater blanket and rim material are bright. We discern two bright units (very bright, “14,” and bright, category “15”). Unlike VIMS data for Selk, the ISS reflectance map features several areas where the contrast between dunes and interdunes is sufficient or nearly sufficient (“12” and “13,” respectively) to exhibit linear bright-dark contrasts that trend in the direction of the dunes resolved by SAR. “Nearly sufficient” in this case signifies that the classification is of less confidence as we are

working at the limits of resolution and contrast. Given the relative darkness of some interdunes compared to nearby bright terrains, we also identified grid cells where dunes were resolved with particularly dark interdunes (“2”) or, more often, grid cells where the overall albedo is similar to the dunes but no dunes are resolved (“4”).

The result largely agrees with the VIMS map, as one might expect, with finer detail captured with higher spatial sampling. Together, the VIMS, and ISS data sets complement the RADAR data by providing broader coverage and information about surface composition.

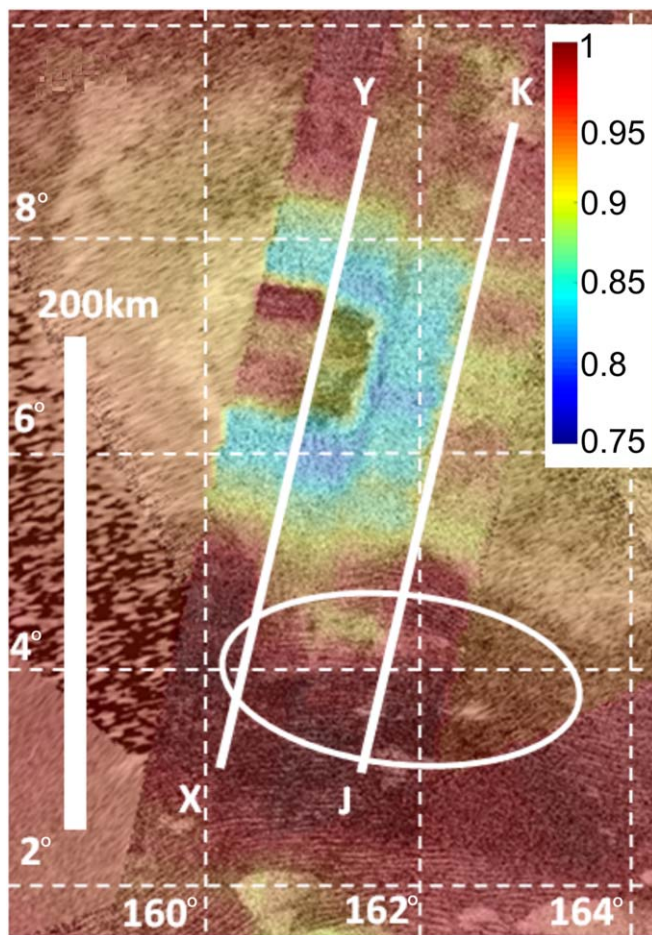


Figure 11. Radar mosaic of Figure 7 shaded with a color relating to the microwave emissivity (Janssen et al. 2016). The blue color indicates a low emissivity also seen at other fresh Titan impact craters, suggestive of a water ice-rich ejecta. The two SARtopo track locations (YX and KJ) and a candidate delivery ellipse are outlined in white. The ellipse placement yields 100% chance of landing on VIMS “Brown” unit suggesting sand cover; the corresponding ISS “dark” material covers 95% of the ellipse, and 93% is in the SAR-classified “dunes” unit.

2.4. Microwave Radiometry and SARtopo

The T95 SAR swath provides additional information beyond the high-resolution radar image. The swath is formed from the union of five subswaths generated by switching in rapid succession between the five feeds to the high-gain antenna. Where these swaths overlap, the same terrain is viewed at different angular positions in the respective beams, and matching their intensity allows an estimate of the terrain height to be made. The effective horizontal resolution, determined by the size of the correlation window, is of the order of 10 km, although the profile data product is sampled more frequently.

Figure 11 shows the location of the two SARtopo tracks plotted in Figure 12 (Neish et al. 2018; Hedgpeeth et al. 2020). Track XY crosses the crater almost diametrically. The crater floor is only 100–200 m below the surrounding terrain, and the rim rises on both sides to about 200 m above the surrounds. The rim slope appears to be only about 3° in the profile, although locally steeper and shallower slopes doubtless exist at smaller scale. As discussed in Shepard et al. (2001), fractal topography with a Hurst exponent of 0.5 typical of natural

planetary surfaces means that reducing the length scale by a factor of ~ 10 reduces the root-mean-square surface height variation by a factor of ~ 3 . Thus, despite the limited horizontal resolution of the SARtopo profile, there are unlikely to be “unseen mountains” with heights larger than shown. However, the *slope* distribution at the lander scale will be rather larger than the profile suggests. The existence of flat areas, however, is expected on the basis of geological analogy—see next section. A 30 km wide, 200 m deep valley appears to be present about 50 km into the track. Track JK, across the outer margin of the morphologically identified ejecta, shows only a minimal topographic signature (~ 100 m) of a “bench.”

The emissivity shown in Figure 11 is derived from the microwave brightness temperature. The radar receiver can estimate the power radiated in the real aperture of each of the five beams. Since the T95 Selk observation was near closest approach, the beam footprint was usefully small (~ 10 km wide) allowing the ejecta blanket and crater to be resolved. As observed at other craters, low brightness temperatures yield low emissivities in the ejecta blanket, suggesting a water ice-rich composition (Janssen et al. 2016; Werynski et al. 2019).

3. Lander Targeting

A full discussion of the operations concept and traverse plan for Dragonfly is beyond the scope of the present paper and will almost certainly evolve over time. It suffices to note here that the initial landing would take place among the dunes where a safe interdune landing site can be determined autonomously after the atmospheric entry and parachute descent. After initial science observations over several Tsols (Titan days: 1 Tsol ~ 16 Earth days), Dragonfly would make initial short “hops” of hundreds of meters to a few kilometers to explore different surface types, such as the shallow dune plinths that typically flank linear dunes. Then, over the following 2 yr or more, longer flights would be made to reconnoiter, and then if judged suitable, land at additional sites progressively toward Selk—see e.g., (Lorenz 2020).

As with the Huygens probe, and the proposed Titan Mare Explorer (and indeed Venus probes, Lorenz 2015), the size of the “landing ellipse” (the area within which the lander is expected to be delivered with some high probability, typically 99%) is driven largely by uncertainty in the zonal winds to be encountered during the long parachute descent. This makes the ellipse wider in the east–west direction than north–south. The north–south dimension is determined in part by the much smaller (but nondeterministic) meridional winds, as well as by the projection of the interplanetary delivery uncertainty onto Titan’s globe and by small uncertainties in entry system drag performance, atmospheric density etc.

Following previous work on specifying a Titan wind model for high latitudes (Lorenz et al. 2012), an engineering wind model was formulated by examining predictions from several Global Circulation Models (e.g., Lora et al. 2019), as well as the wind profile developed from Doppler tracking of the Huygens probe, and Cassini observations of temperature contrasts from which zonal winds can be estimated. Monte Carlo simulations of the entry and descent were performed at NASA’s Langley Research Center using the POST II (Program to Optimize Simulate Trajectories) simulation tool, widely used in EDL analyses on Mars and other missions. These simulations yielded an ellipse of 148.9×72.0 km, centered at

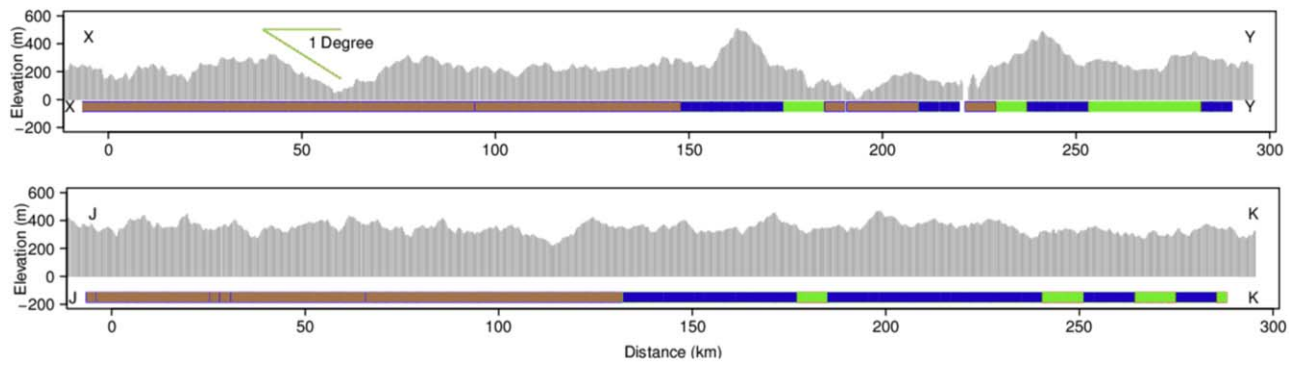


Figure 12. T95 SARTopo profiles outlined in Figure 11. *XY* shows the rim and floor of the crater (150–250 km) and the nearby ejecta blanket while *JK* passes over the “bench” identified by Soderblom et al. (2010). The color strips beneath the profile show the VIMS terrain classification along the profile.

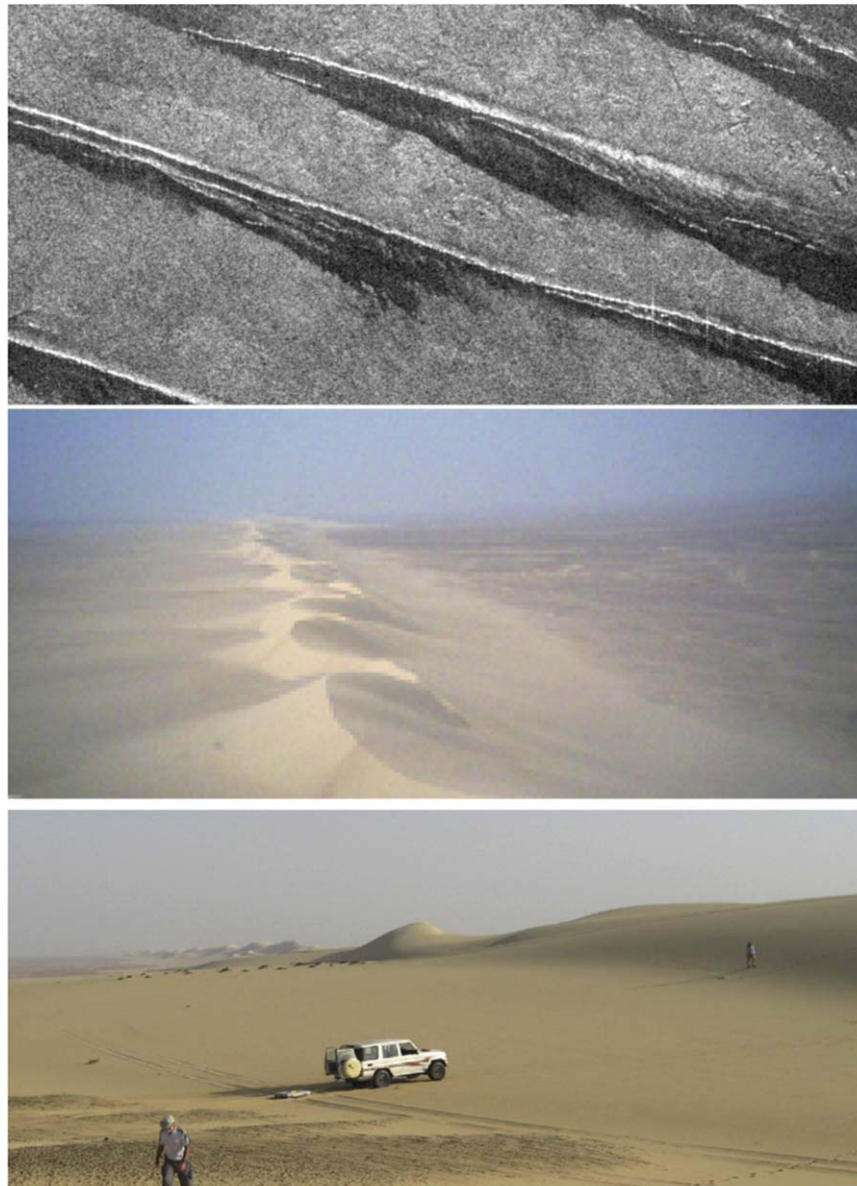


Figure 13. (Top) Tapering linear dunes in Egypt, morphologically identical in radar images (XSAR) with the dunes seen to the Southeast of Selk. (Middle) Kiteborne camera view of Ghard el Quattaniya linear dunes west of Cairo, Egypt showing dune and plinth. (Bottom) Field photo at same dune showing Ground Penetrating Radar operations. While dune slopes themselves would be avoided, it is clear that shallow-sloped dune plinths can allow safe access to sand material. (Photos: Lorenz).



Figure 14. Field photographs from the Haughton impact structure. Although steep slopes exist, flat areas of sand and gravel permit even fixed-wing aircraft to find landing sites. (Photos: Neish).

3.72°N , 161.8°E for lander separation from its parachute. (This occurs at ~ 1 km height: the landing itself involves a short horizontal flight that is not modeled in this calculation.) Although retargeting may demand an eventual end-to-end reanalysis, in practice the coupling between the nominal aimpoint (the center of the ellipse) and the various error terms is very weak over the distances considered here (just a few degrees of latitude or longitude). The ellipse can thus be translated more or less unchanged over small distances as the mission parameters, or interpretations of remote sensing data, are refined.

The ellipse (coincidentally almost exactly the same size as the Viking lander ellipses, e.g., Stooke (2012), albeit for rather different reasons) was positioned to the southeast of the crater, since this area had direct topographic information and dunes that were well-resolved in SAR and close to the crater. For the purpose of Phase A mission definition, the ellipse was positioned as close to the crater as possible, while retaining a better than 95% chance of being on the VIMS “brown unit” and 95% on ISS-dark (thus likely sand-covered) terrain. Clearly, relaxation or tightening of such constraints could allow the ellipse to be shifted by perhaps a few tens of kilometers. In the limit, one could center the landing footprint on Selk itself, but the ellipse is large enough that it would include a substantial fraction of rim and ejecta terrains, in contiguous regions that might be too large to fly across.

4. Terrestrial Analogs

Terrestrial analogs to Titan’s dune fields are well-established. Key in the recognition of this landscape on Titan were the morphological similarities to the linear dunes in terrestrial sand seas, notably the Namib and Arabian deserts (Lorenz et al. 2006; Radebaugh et al. 2008).

Of particular relevance in the target area chosen is that dunes “peter out,” forming slender dark triangles—see the upper panel of 13. This is symptomatic of weaker sand supply and indicates an increased likelihood that at least some sand-free patches may be encountered (recognizing that the VIMS and ISS data sets here suggest that overall the surface here is generally sand-covered, or at least sand-colored). It further argues that the dunes will likely not be as tall as those observed

in the center of some of the major sand seas (e.g., the 160 m high dunes seen in Belet determined by radarclinometry in Lorenz et al. 2006 or the 60–120 m dunes in Fensal measured by altimetry in Mastrogiuseppe et al. 2014).

A good analog of these terminal linear dunes are those seen at Quatanniya in the eastern margins of the desert in northern Egypt. These, described by desert forces in World War II (Lorenz 2011) as “saw-toothed sand peaks like a string of battleships in line ahead at sea... appearing and disappearing over the rolling gravel” are a few tens of meters in height, with wide, shallow dune plinths. Figure 13 shows the field appearance of these features, and radar characteristics of similar dunes farther south (which were the subject of a backscatter modeling study by Paillou et al. 2014). The wide dune plinths are shallow in slope, permitting landings to access sand material without confronting the steep slopes of the crest.

Perhaps the best terrestrial analog to a large relatively fresh Titan crater like Selk is the Haughton Impact Structure in Northern Canada, shown in Figure 14 (Neish et al. 2018). Although rather smaller (20 km diameter versus 80 km for Selk), Haughton has only moderate modification, mostly by fluvial and periglacial processes. Morphological evidence suggests a similar modification state at Selk: the crater rim and ejecta blanket are still intact but interrupted by fluvial networks. Furthermore, recent analysis of compositional data from VIMS and microwave radiometry led Werynski et al. (2019) to classify Selk as an intermediate-aged crater. By analogy with Haughton, then, steep slopes, especially at the crater rim, are anticipated but so are flat areas. Landing and sampling of the sand and/or gravel clasts present should be possible.

Another analog is the 5.5 km Waqf As Suwwan impact structure (Salameh et al. 2008) in Jordan (Figure 15). Although an even smaller analog, its desert setting and subdued topography (the crater has an age of 35 Myr, so has been modified by erosion and deposition) gives a sense of how Titan craters might appear. The rim height is around 100 m above the floor, compared with 400 m for Selk, but since Selk is about 12 times larger and the width of the wall correspondingly broader, the slopes on Selk will be generally shallower than those at Waqf As Suwwan. The crater floor there is generally desert pavement, thus providing further evidence for ample safe landing sites at Selk.



Figure 15. Field panorama of the Waqf As Suwwan impact structure from the rim, which can be seen extending to the right. The central uplift is visible at center, but overall the topography is very subdued. (Photo: Lorenz).







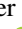

5. Conclusion

While no single area represents the full diversity of Titan's surface features, the Selk impact structure offers a variety of surface compositions and geological settings over modest distances. Organic materials are available via the dune sands (and, potentially, the VIMS green unit) while water ice-rich material should be available at the ejecta blanket (and perhaps also at bedrock exposed in the interdunes). Crater materials are especially desirable targets due to the strong promise of sampling where liquid water and organics have interacted. In addition to impact-associated processes, this region has been worked by the aeolian and fluvial processes known to operate across Titan.

Terrestrial analog craters in fact suggest that even aiming Dragonfly directly at the crater on arrival would *probably* result in finding a safe landing. However, landing first in the dunes and then exploiting Titan's environment for easy aerial mobility offered a logical and easily communicated strategy to minimize risk while maximizing the potential for scientific exploration.

The work at APL was supported by the Dragonfly Phase A study award from the NASA New Frontiers Program. We thank Chris Scott and Marty Ozimek of APL for devising the delivery trajectory, Douglas Adams of APL for definition of the aerothermodynamic constraints, and Joseph White of NASA's Langley Research Center for computing the delivery ellipse. Philippe Paillou provided the XSAR image. The first author's field work in Egypt was supported by the Cassini RADAR team. We thank Léa Bonnefoy and Alex Hayes for pointers on Cassini RADAR data. C. N. acknowledges support from the Canadian Space Agency for field work at the Houghton Impact Structure.

ORCID iDs

Ralph D. Lorenz  <https://orcid.org/0000-0001-8528-4644>
 Shannon M. MacKenzie  <https://orcid.org/0000-0002-1658-9687>
 Catherine D. Neish  <https://orcid.org/0000-0003-3254-8348>
 Alice Le Gall  <https://orcid.org/0000-0002-9023-4868>
 Elizabeth P. Turtle  <https://orcid.org/0000-0003-1423-5751>
 Jason W. Barnes  <https://orcid.org/0000-0002-7755-3530>
 Melissa G. Trainer  <https://orcid.org/0000-0003-1106-8580>
 Erich Karkoschka  <https://orcid.org/0000-0002-4165-0064>

References

Barnes, J. W., Brown, R. H., Soderblom, L., et al. 2007, *Icar*, **186**, 242
 Barnes, J. W., Brown, R. H., Soderblom, L., et al. 2008, *Icar*, **195**, 400
 Barnes, J. W., MacKenzie, S. M., Young, E. F., et al. 2020, *PSJ*, **1**, 24
 Bonnefoy, L. E., Hayes, A. G., Hayne, P. O., et al. 2016, *Icar*, **270**, 222

Brossier, J. F., Rodriguez, S., Cornet, T., et al. 2018, *JGRE*, **123**, 1089
 Corlies, P., Hayes, A., Birch, S., et al. 2017, *GeoRL*, **23**, 11,754
 Golombek, M. P., Grant, J. A., Parker, T. J., et al. 2003, *JGRE*, **108**, 8072
 Griffith, C. A., Pentead, P. F., Turner, J. D., et al. 2019, *NatAs*, **3**, 642
 Hedgepeth, J. E., Neish, C. D., Turtle, E. P., et al. 2020, *Icar*, **344**, 113664
 Hofgartner, J. D., Hayes, A. G., Campbell, D. B., et al. 2020, *NatCo*, **11**, 2829
 Janssen, M. A., Le Gall, A., Lopes, R. M., et al. 2016, *Icar*, **270**, 443
 Karkoschka, E., McEwen, A., & Perry, J. 2017, *LPSC*, **48**, 2518
 Lebreton, J.-P., Witasse, O., Sollazzo, C., et al. 2005, *Natur*, **438**, 758
 Le Gall, A., Janssen, M., Wye, L., et al. 2011, *Icar*, **213**, 608
 Lopes, R. M. C., Malaska, M. J., Schoenfeld, A. M., et al. 2019, *NatAs*, **4**, 228
 Lora, J. M., Tokano, T., Vatant d'Ollone, J., Lebonnois, S., & Lorenz, R. D. 2019, *Icar*, **333**, 113
 Lorenz, R. D. 2011, *AeoRe*, **3**, 229
 Lorenz, R. D. 2015, *P&SS*, **108**, 66
 Lorenz, R. D. 2019, *AdSpR*, **64**, 944
 Lorenz, R. D. 2020, *AdSpR*, **65**, 1383
 Lorenz, R. D., Newman, C. E., Tokano, T., et al. 2012, *P&SS*, **70**, 73
 Lorenz, R. D., Turtle, E. P., Barnes, J. W., et al. 2018, *JHATD*, **34**, 374, https://dragonfly.jhuapl.edu/News-and-Resources/docs/34_03-Lorenz.pdf
 Lorenz, R. D., Wall, S., Radebaugh, J., et al. 2006, *Sci*, **312**, 724
 Mastrogiuseppe, M., Poggiali, V., Seu, R., Martufi, R., & Notarnicola, C. 2014, *Icar*, **230**, 191
 Masursky, H., & Crabill, N. 1976, *Sci*, **193**, 809
 Neish, C., Somogyi, A., Imanaka, H., Lunine, J., & Smith, M. 2008, *AsBio*, **8**, 273
 Neish, C. D., Barnes, J. W., Sotin, C., et al. 2015, *GeoRL*, **42**, 3746
 Neish, C. D., & Lorenz, R. D. 2012, *P&SS*, **60**, 26
 Neish, C. D., Lorenz, R. D., Turtle, E. P., et al. 2018, *AsBio*, **18**, 571
 Neish, C. D., Somogyi, Á., Lunine, J. I., & Smith, M. A. 2009, *Icar*, **201**, 412
 Neish, C. D., Somogyi, Á., & Smith, M. A. 2010, *AsBio*, **10**, 337
 Ott, S. 1992, in IAF Int. Astronautical Congress 43 (Washington, DC: IAF), 10
 Paillou, P., Bernard, D., Radebaugh, J., et al. 2014, *Icar*, **230**, 208
 Porco, C. C., Baker, E., Barbara, J., et al. 2005, *Natur*, **434**, 159
 Radebaugh, J., Lorenz, R. D., Kirk, R. L., et al. 2007, *Icar*, **192**, 77
 Radebaugh, J., Lorenz, R. D., Lunine, J. I., et al. 2008, *Icar*, **194**, 690
 Rodriguez, S., Garcia, A., Lucas, A., et al. 2014, *Icar*, **230**, 168
 Salameh, E., Khoury, H., Reimold, W. U., & Schneider, W. 2008, *M&PS*, **43**, 1681
 Scott, C. J., Ozimek, M. T., Adams, D. S., et al. 2018, in AAS/AIAA Astrodynamics Specialist Conf. (Pasadena, CA: JPL, NASA), <http://hdl.handle.net/2014/48626>
 Shepard, M. K., Campbell, B. A., Bulmer, M. H., et al. 2001, *JGR*, **106**, 32777
 Soderblom, J. M., Brown, R. H., Soderblom, L. A., et al. 2010, *Icar*, **208**, 905
 Soderblom, L. A., Kirk, R. L., Lunine, J. I., et al. 2007, *P&SS*, **55**, 2025
 Solomonidou, A., Neish, C., Coustenis, A., et al. 2020, *A&A*, **641**, A16
 Stiles, B. W., Hensley, S., Gim, Y., et al. 2009, *Icar*, **202**, 584
 Stefan, E., Lorenz, R., Lunine, J., et al. 2013, in IEEE Aerospace Conf. (Piscataway, NJ: IEEE), 211
 Stooke, P. J. 2012, *The International Atlas of Mars Exploration: Vol. 1, 1953 to 2003: The First Five Decades* (Cambridge: Cambridge Univ. Press)
 Turtle, E. P., Barnes, J., Trainer, M., et al. 2018, *LPSC*, **49**, 1641
 Werynski, A., Neish, C. D., Gall, A. L., & Janssen, M. A. 2019, *Icar*, **321**, 508
 West, R., & Veeramachaneni, C. 2014, *RADAR Titan Flyby during S80/T95*, Cassini RADAR Team, https://pdsimage2.wr.usgs.gov/archive/co-v_e_j_s-radar-3-sbdr-v1.0/CORADR_0253_V03/EXTRAS/T95_SEQUENCE_DESIGN_MEMO.PDF
 Wood, C. A., Lorenz, R., Kirk, R., et al. 2010, *Icar*, **206**, 334